

THE HOST GALAXY AND THE EXTENDED EMISSION-LINE REGION OF THE RADIO GALAXY 3C 79¹

HAI FU AND ALAN STOCKTON

Institute for Astronomy, University of Hawaii, Honolulu, HI 96822; fu@ifa.hawaii.edu, stockton@ifa.hawaii.edu

Received 2007 October 10; accepted 2007 December 26

ABSTRACT

We present extensive ground-based spectroscopy and *HST* imaging of 3C 79, an FR II radio galaxy associated with a luminous extended emission-line region (EELR). Surface brightness modeling of an emission-line-free *HST* *R*-band image reveals that the host galaxy is a massive elliptical with a compact companion 0''.8 away and 4 magnitudes fainter. The host galaxy spectrum is best described by an intermediate-age (1.3 Gyr) stellar population (4% by mass), superimposed on a 10 Gyr old population and a power law ($\alpha_\lambda = -1.8$); the stellar populations are consistent with super-solar metallicities, with the best fit given by the 2.5 Z_\odot models. We derive a dynamical mass of $4 \times 10^{11} M_\odot$ within the effective radius from the velocity dispersion. The EELR spectra clearly indicate that the EELR is photoionized by the hidden central engine. Photoionization modeling shows evidence that the gas metallicity in both the EELR and the nuclear narrow-line region is mildly sub-solar ($0.3 - 0.7 Z_\odot$) — significantly lower than the super-solar metallicities deduced from typical active galactic nuclei in the Sloan Digital Sky Survey. The more luminous filaments in the EELR exhibit a velocity field consistent with a common disk rotation. Fainter clouds, however, show high approaching velocities that are uncoupled with this apparent disk rotation. The striking similarities between this EELR and the EELRs around steep-spectrum radio-loud quasars provide further evidence for the orientation-dependent unification schemes. The metal-poor gas is almost certainly not native to the massive host galaxy. We suggest that the close companion galaxy could be the tidally stripped bulge of a late-type galaxy that is merging with the host galaxy. The interstellar medium of such a galaxy is probably the source for the low-metallicity gas in 3C 79.

Subject headings: galaxies: active — galaxies: abundances — galaxies: individual (3C 79) — galaxies: interactions — galaxies: ISM

1. INTRODUCTION

Low-redshift quasars are often surrounded by massive ionized nebulae showing filamentary structures on scales of a few tens of kpcs. More specifically, about 40% of the quasars at $z < 0.5$ that are also steep-spectrum (i.e., usually FR II type) radio sources show such extended emission-line regions (EELRs) with an [O III] $\lambda 5007$ luminosity greater than 4×10^{41} erg s⁻¹. Here we will focus our discussion on these steep-radio-spectrum quasars, because (1) they are possibly the counterparts of FR II radio galaxies like 3C 79, and (2) the presence of a powerful radio jet seems to be a necessary (though not sufficient) condition for producing a luminous EELR, as implied by the correlation between radio spectral index and extended optical emission (Boroson & Oke 1984; Stockton & MacKenty 1987).

An EELR typically has a mass of $10^{9-10} M_\odot$, displays globally disordered kinematics, and shows a complex morphology that bears no obvious relationships either with the host galaxy

or with the extended radio structure (Stockton & MacKenty 1987; Fu & Stockton 2006, 2007b; see Stockton et al. 2006 for a review). In terms of quasar luminosity, host galaxy luminosity, and black hole mass, the quasars that show EELRs (hereafter the “EELR quasars”) do not differ significantly from non-EELR quasars. But the former are all low-metallicity quasars. The gas metallicity in their broad-line regions (BLRs) is significantly lower ($\lesssim 0.6 Z_\odot$) than that of non-EELR quasars ($> Z_\odot$) (Fu & Stockton 2007a). Although this gas-phase metallicity is unexpectedly low for galaxies with the masses found for these quasar hosts, it is consistent with that in their EELRs. Combining all of the pieces together, the most likely scenario for the origin of an EELR is that it comprises gas that is native to a gas-rich galaxy that merged with the quasar host and triggered the quasar activity, after which a large fraction of the gas was impulsively swept out by a large-solid-angle blast wave (i.e., a superwind), in a manner similar to that envisioned for quasar-mode feedback in the early universe (e.g., Di Matteo et al. 2005).

3C 79 ($z = 0.256$, $1'' = 4$ kpc)² is a narrow-line radio galaxy having FR II radio jets with a central component (Hes et al. 1995; Spangler et al. 1984; Hardcastle et al. 1997). *Hubble Space Telescope* (*HST*) WFPC2 broad-band images show a complex optical morphology — a bright elliptical galaxy with an effective radius of 7.5 kpc, accompanied by multiple “tidal arms” and two distinct “cores” other than the nucleus (Dunlop et al. 2003; de Koff et al. 1996). As we will show in § 3.1, only the galaxy and the “core” southwest of the nucleus are true continuum sources; the rest are all line-emitting regions. The nuclear spectra of 3C 79 show

¹ Based in part on observations obtained at the Gemini Observatory, which is operated by the Association of Universities for Research in Astronomy, Inc., under a cooperative agreement with the NSF on behalf of the Gemini partnership: the National Science Foundation (United States), the Particle Physics and Astronomy Research Council (United Kingdom), the National Research Council (Canada), CONICYT (Chile), the Australian Research Council (Australia), CNPq (Brazil) and CONICET (Argentina). Gemini Program ID: GN-2006B-C-3. Some of the data presented herein were obtained at the W.M. Keck Observatory, which is operated as a scientific partnership among the California Institute of Technology, the University of California and the National Aeronautics and Space Administration. The Observatory was made possible by the generous financial support of the W.M. Keck Foundation. Based also in part on observations made with the NASA/ESA Hubble Space Telescope, obtained from the Data Archive at the Space Telescope Science Institute, which is operated by the Association of Universities for Research in Astronomy, Inc., under NASA contract NAS 5-26555.

² Throughout we assume a flat cosmological model with $H_0 = 70$ km s⁻¹ Mpc⁻¹, $\Omega_m = 0.3$, and $\Omega_\Lambda = 0.7$

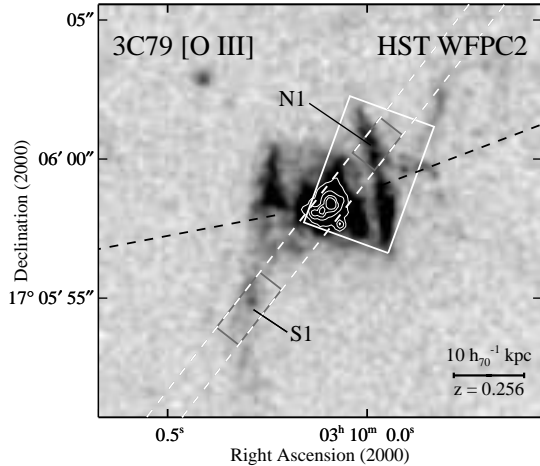


FIG. 1. — *Hubble Space Telescope* (HST) WFPC2 FR680N [O III] image of 3C 79. Superimposed are contours from the continuum dominated WFPC2 F675W image, at levels of $1.6 \times 10^{-17} \times (1, 1.53, 2.34, 3.57)$ $\text{erg cm}^{-2} \text{s}^{-1} \text{\AA}^{-1} \text{arcsec}^{-2}$ above the background, showing the structures near the nucleus. Also overlaid are the field of the GMOS/IFU (white rectangular box) and the position of the LRIS slit (white dashed lines; PA = 142°). The extraction apertures for the N1 and S1 regions are shown with grey boxes. The FR II radio jet directions are indicated by the black dashed lines. The angular size of the scale bar is $2''.51$. North is up and east is to the left for this and the following HST images.

stellar absorption lines and a red continuum, indicating an old stellar population (Miller 1981; Boroson & Oke 1987). A line-emitting region in a curving filament extending $12''$ to the northwest of the galaxy was seen in an $\text{H}\alpha$ image and was subsequently confirmed by a slit spectrum covering the [O III] $\lambda\lambda 4959, 5007$ region (McCarthy et al. 1995, 1996). The spectrum also shows emission-line clouds between the filament and the nucleus, as well as clouds extending $5''$ to the southeast. An [O III] $\lambda 5007$ image taken in much better seeing (Stockton et al. 2006) shows a very rich morphology and an emission-line luminosity comparable to that of the EELRs around steep-spectrum radio-loud quasars, establishing that 3C 79 is associated with an EELR.

In line with the orientation-based unification schemes of FR II radio galaxies and radio-loud quasars (Barthel 1989), we believe that 3C 79 belongs to the same class of object as the EELR quasars, such as 3C 249.1 and 4C 37.43, but it is viewed at a different angle with respect to the molecular torus surrounding the central engine. If this is true, then the unique geometry of radio galaxies like 3C 79 could afford us a natural coronagraph blocking the blinding glare from the central engine. Such objects can be especially useful for studies of their host galaxies, which potentially preserve a large amount of information regarding the forces that have sculpted these spectacular emission-line regions.

In this paper, we study the host galaxy and the EELR of 3C 79 with extensive ground-based spectroscopy in combination with a re-analysis of archival HST WFPC2 multi-band images. First, we briefly describe our observations and data reduction procedures in § 2. In § 3 we study the morphology, stellar kinematics and stellar populations of the host galaxy. We then demonstrate the similarities between the 3C 79 EELR and the ones around quasars, in terms of gas kinematics, pressure, ionization mechanism, and metallicity in § 4. Finally, we discuss our main results in § 5 and close with a summary in § 6.

2. OBSERVATIONS AND DATA REDUCTION

2.1. GMOS Integral Field Spectroscopy

We observed 3C 79 with the Integral Field Unit (IFU; Allington-Smith et al. 2002) of the Gemini Multiobject Spectrograph (GMOS; Hook et al. 2004) on the Gemini North telescope. The observations were performed on the night of 2006 December 21 (UT). Three exposures of 2880 s were obtained using the half-field mode with the B600/G5303 grating at a central wavelength of 6242\AA . With this setting, we had a field-of-view (FOV) of $3''.5 \times 5''$, a wavelength range of 4100 to 6900\AA , a dispersion of $0.46 \text{\AA pixel}^{-1}$ and an instrumental full width at half-maximum (FWHM) of 4.5 pixels (2.1\AA). The host galaxy was placed at the lower-left corner of the IFU field so that a large fraction of the western part of the EELR could be covered (Figure 1). Feige 34 was observed for flux calibration.

The data were reduced using the Gemini IRAF package (Version 1.8). The data reduction pipeline (GFREDUCE) consists of the following standard steps: bias subtraction, spectral extraction, flat-fielding, wavelength calibration, sky subtraction, and flux calibration. Cosmic ray rejection was performed by L.A.Cosmic (van Dokkum 2001) before running the data through the reduction pipeline, with careful adjustment of the parameters to avoid misidentification of real data. Spectra from different exposures were assembled and resampled to construct individual data cubes (x, y, λ) with a pixel size of $0''.05$ (GFCUBE). To correct for the differential atmosphere refraction (DAR), we first binned the data cubes along the wavelength direction to increase the S/N ratio of the host galaxy; then the centroid of the galaxy was measured for each bin, and a polynomial was fit to the (x, y) coordinates, restricted by the fact that DAR only causes the centroids to vary along a straight line in (x, y) plane (at the parallactic angle); finally we shifted the image slices at each wavelength using the solution from the polynomial fit. The three data cubes were then combined and binned to $0''.2$ pixels, the original spatial sampling of the IFU fiber-lenslet system, to form the final data cube.

2.2. LRIS Long-Slit Spectroscopy

We obtained optical long-slit spectroscopy of 3C 79 on the night of 2007 October 17 (UT) with the Low Resolution Imaging Spectrograph (Oke et al. 1995) on the Keck I telescope. The Cassegrain Atmospheric Dispersion Compensator (Cass ADC³) was used during the observation. We took two 1200 s exposures through a $1''$ slit centered on the nucleus at a position angle of 142° (Fig. 1). On the blue arm we used the 600 groove mm^{-1} grism blazed at 4000\AA , whilst on the red arm we used the 400 groove mm^{-1} grating blazed at 8500\AA , offering, respectively, wavelength ranges of $3100\text{--}5600 \text{\AA}$ and $5100\text{--}8900 \text{\AA}$ and spectral resolutions of 4 and 7\AA (FWHM). The spectra were taken at low airmass (~ 1.1), and the seeing was about $0''.7$ throughout the night.

The spectra were reduced in the standard fashion using IRAF tasks. The blue-arm spectra were wavelength-calibrated using observations of arc lamps, whilst for the red-arm spectra we used night-sky lines. Background sky was removed by fitting low-order cubic splines to the regions on each side of the object along the slit direction using BACKGROUND. One-dimensional spectra of 3C 79 were

³ <http://www2.keck.hawaii.edu/inst/adc/docs/>

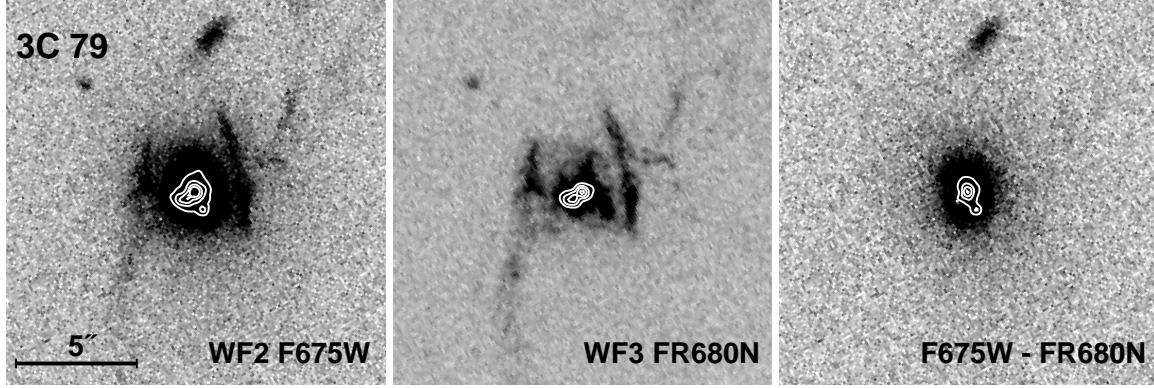


FIG. 2.— *HST* WFPC2 images of 3C 79: (left) the F675W image, (middle) the FR680N [O III] image rotated, shifted and scaled to match the F675W image, (right) the residual from subtracting the FR680N [O III] image off the F675W image. The contours, which are from the same images but smoothed by a Gaussian function with a FWHM of 3 pixels, show the central high surface brightness features. Contour levels are the same as in Fig. 1.

first extracted with a wide ($11''$) aperture, and they were flux-calibrated and corrected for atmospheric absorption using the spectrophotometric standard Wolf 1346 (taken 5 min after the nautical twilight earlier in the night). The calibrated spectra from the two arms agree perfectly in their overlapping region. Then, one-dimensional spectra of high S/N ratio were obtained by using a $2''$ extraction aperture. These spectra were multiplied by appropriate smooth curves so that their continua match those of the wide-aperture spectra. Finally, the blue and the red sides, after flux calibration and atmospheric absorption correction, were joined and binned to a common linear dispersion (1.86 \AA per pixel) using SCOMBINE. The line-of-sight Galactic reddening ($A_V = 0.421$, Schlegel et al. 1998) was corrected with a standard reddening curve (Cardelli et al. 1989). We obtained an absolute flux calibration by scaling the spectrum to the *HST* photometry result from § 3.1 ($F_\lambda = 1.8 \times 10^{-16} \text{ erg cm}^{-2} \text{ s}^{-1} \text{ \AA}^{-1}$ between 6300 and 7300 \AA).

2.3. *HST* WFPC2 Imaging

To study the host galaxy morphology, we obtained WFPC2/WFC F675W ($4 \times 565 \text{ s}$) and FR680N ($2 \times 1300 \text{ s}$) images, and a WFPC2/PC F702W ($2 \times 140 \text{ s}$) image of 3C 79, available from the archive of the *HST*. The two broad-band images have been previously presented by Dunlop et al. (2003) and de Koff et al. (1996). The Linear Ramp Filter (LRF; FR680N) image has a central wavelength of 6284 \AA and a bandpass FWHM of 82 \AA at the position of 3C 79, i.e., the filter is centered on the redshifted [O III] $\lambda 5007$ emission line. Images observed with LRFs are not flat-field calibrated in the calibration pipeline, so we flattened the LRF image with an F631N flat field reference image.

Additional cosmic rays after the standard pipeline reduction were identified and replaced by L.A.Cosmic (van Dokkum 2001), again with careful adjustment of the parameters to avoid misidentification of real data.

3. THE HOST GALAXY

3.1. Galaxy Morphology

Though the WFC2 F675W image is dominated by continuum radiation, H β and [O III] $\lambda\lambda 4959, 5007$ lines fall on the shortward wing of the filter profile, where the transmissions are about 42, 76, and 85%, respectively. To study the morphology of the host galaxy, one has to remove the line-emitting regions from the image. We thus rotated the WFC3 LRF [O III] image to the orientation of the F675W image,

shifted and scaled the image to match the F675W image, and finally subtracted it off the wide-band image to obtain an emission-line free image (hereafter the “F675W*” image; Fig. 2). A close companion $0''.8$ southwest of the major host galaxy is seen in the F675W* image, which we designate as 3C 79A. The host galaxy itself is simply called 3C 79 in this section.

3C 79A is better sampled in the PC1 F702W image, so we used this image to study its morphology. We used C. Y. Peng’s GALFIT software (Peng et al. 2002) to fit the two-dimensional galaxy profile, and we used an oversampled Tiny Tim⁴ PSF. The result is shown in Fig. 3. As indicated by the best fit Sérsic index of $n = 1.23$, the profile is close to an exponential. As shown by the residuals, the exponential model clearly provides a better fit than the de Vaucouleurs model.

We chose to use the F675W* image to study the morphology of 3C 79. We converted the geometric parameters from the best fit exponential model of 3C 79A (effective radius, axis ratio, and position angle [PA]) to the WFC image, and froze them; however, we allowed the position and magnitude of 3C 79A vary in the modeling of 3C 79. Figure 4 shows that 3C 79 can be described by a de Vaucouleurs model, as indicated by the high Sérsic index. Table 1 summarizes the morphology results. The PA of the minor axis of 3C 79 is aligned within 5° to the direction of the radio jets (as defined by the hot spots; see Fig. 1). The companion galaxy 3C 79A is located $0''.84$ (3.3 kpc) southwest of 3C 79, and its PA is aligned within 7° to the direction of the host galaxy.

Dunlop et al. (2003) modeled the 3C 79 host galaxy with a de Vaucouleurs model (plus a concentric PSF to account for the narrow-line region [NLR]). For comparison, their results are also shown in Table 1. Dunlop et al. used the original F675W image, i.e., the emission-line regions were not removed; thus they overestimated the brightness of the galaxy and had a poor estimate for the axis ratio and PA. We were able to reproduce their results using GALFIT when modeling the original F675W image.

3.2. Stellar Kinematics

We extracted the host spectrum from the final combined GMOS data cube using a $0''.5$ (2 kpc) radius aperture⁵. Although the GMOS spectrum shows a poorer S/N ratio in com-

⁴ <http://www.stsci.edu/software/tinytim/tinytim.html>

⁵ We chose such a small aperture because: (1) it yields the best S/N ratio compared to apertures of other sizes; and (2) it avoids hitting the edges of the FOV at short wavelengths

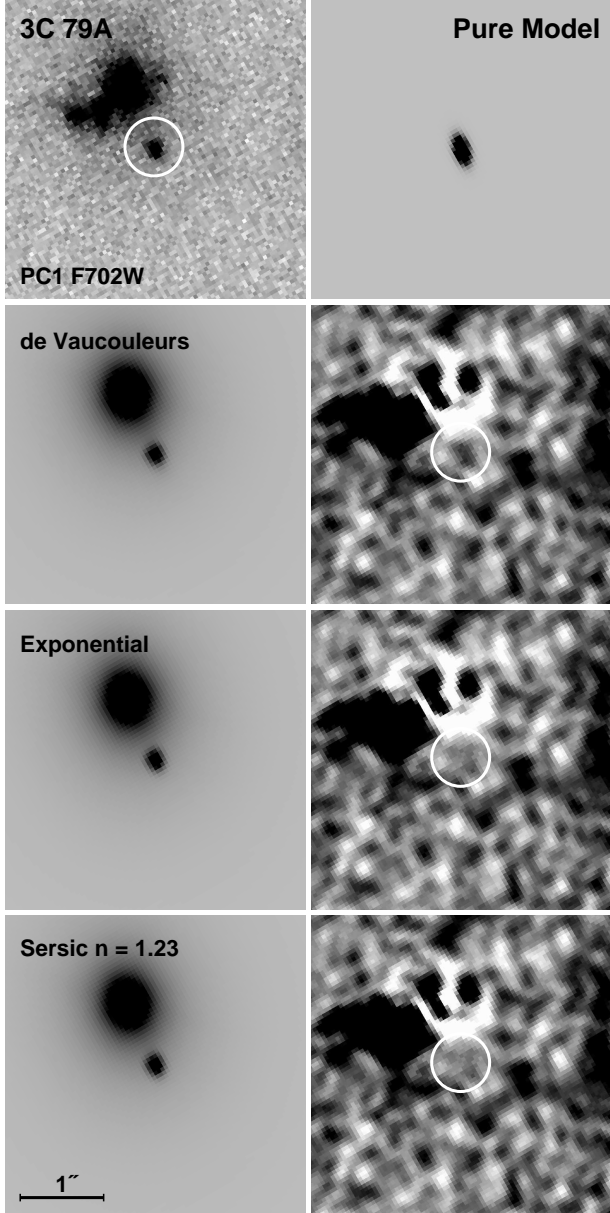


FIG. 3.— Two-dimensional modeling of the close companion galaxy 3C 79A. The top left panel shows the original WFPC2/PC1 F702W image. Directly below are best fit de Vaucouleurs (“ $r^{1/4}$ law”), exponential, and Sérsic models convolved with the PSF. To remove the light from the host galaxy and the nuclear NLR, we fitted a de Vaucouleurs plus PSF, and the best fit models are shown together with the 3C 79A models. To the right of each model are shown the smoothed residuals after subtracting the models. The residuals are displayed at a higher contrast. The top right panel shows the best fit Sérsic model without convolution with the PSF, which gives the best realization of the gross morphology of the galaxy. The white circles in some panels are centered at the position of 3C 79A and have a radius of $0''.35$.

parison with the LRIS spectrum, it has a better spectral resolution (2.1 \AA FWHM as opposed of 7 \AA), making it best-suited for measuring stellar kinematics. We chose to use the stellar synthesis models of Vazdekis (1999) to fit the data. Although these models have very limited spectral coverage compared with those of Bruzual & Charlot (2003), they have a better spectral resolution ($\sim 1.8 \text{ \AA}$), which is similar to that of the GMOS spectrum, and they do cover the spectral region where the spectrum show the highest S/N ratio ($S/N \sim 33$ at rest-frame wavelengths of $4800 \text{ \AA} \leq \lambda_0 \leq 5500 \text{ \AA}$). For

the modeling we used M. Cappellari’s IDL program⁶ implementing the pixel-fitting method of Cappellari & Emsellem (2004). The program finds the best fit to the data by convolving the model templates with a line-of-sight velocity distribution (LOSVD). Since we used a Gaussian function to parameterize the LOSVD, the program reports the mean stellar velocity (V^*) and velocity dispersion (σ^*). In Figure 5 we plot our best fit model against the data. Following Emsellem et al. (2004), we included a multiplicative Legendre polynomial of degree 6 in the fit⁷ to correct the model continuum shape. The kinematics results are insensitive to the assumed model age, although χ^2 increases rapidly for models younger than 3 Gyr and the oldest population yielded the minimum χ^2 . Using a Monte-Carlo approach, we found that the 1σ uncertainties of V^* and σ^* are both about 11 km s^{-1} . These errors should be regarded as lower limits since they do not account for the effect of the template and continuum mismatch. Assuming a negligible amount of systematic rotation, the measured velocity dispersion of $\sim 236 \text{ km s}^{-1}$ implies a virial mass of $5R\sigma^2/G = 1.3 \times 10^{11} M_\odot$ within 2 kpc from the galaxy center. We estimated the luminosity-weighted velocity dispersion within $r_{1/2}$ (7.2 kpc) to be $\sigma_{1/2}^* = 218 \pm 20 \text{ km s}^{-1}$, with the aperture correction function for SAURON elliptical galaxies, $(\sigma_{1/2}^*/\sigma_r^*) = (r_{1/2}/r)^{-0.066 \pm 0.035}$ (Cappellari et al. 2006). The virial mass inside $r_{1/2}$ is then $M_{1/2}^{\text{vir}} = 4.0^{+0.8}_{-0.6} \times 10^{11} M_\odot$.

3.3. Stellar Population

To study the stellar population of the host galaxy, we have performed detailed continuum modeling to the 3C 79 nuclear spectrum obtained from LRIS. The host galaxy shows a strong UV excess (Fig. 6) and a broad (FWHM $\sim 6500 \text{ km s}^{-1}$) Mg II $\lambda 2798$ line (Fig. 7), but no broad H α or H β lines are seen. These characteristics seem to resemble closely the radio galaxy Cygnus A (Antonucci et al. 1994; Ogle et al. 1997), implying a significant scattered quasar component. In addition, stellar absorption features are evident (Ca II K $\lambda 3933$, the G band $\lambda 4300$, and the Mg I b $\lambda 5175$, etc.), implying a dominating old stellar population (OSP). As a first guess, we tried to model the continuum with three components: (1) a nebular continuum (at $T = 10,000, 15,000$, and $20,000 \text{ K}$), (2) a power law ($F_\lambda \propto \lambda^{\alpha_\lambda}$; $-0.4 \leq \alpha_\lambda \leq -1.8$ in accordance with the composite UV/optical quasar spectrum; Vanden Berk et al. 2001), and (3) an OSP ($7 \text{ Gyr} \leq \text{Age} \leq 10 \text{ Gyr}$ ⁸, and $Z = 0.2, 0.4, 1.0$, and $2.5 Z_\odot$; $Z_\odot = 0.02$). The same IDL program was used in the modeling as in the previous section, but this time we did *not* include polynomials to adjust the model continuum shape. Since the nebular continuum scales with the Balmer lines, we required that the H γ flux from the models to be within 5% of the measured flux.

Figure 6a shows the best fit three-component model (i.e., the model that produces the least χ^2), which is a combination of a 9-Gyr-old $2.5 Z_\odot$ population, a nebular continuum at $T = 15,000 \text{ K}$, and a λ^α power law with $\alpha = -1.4$. This model fits both the continuum shape and most of the absorption features, however, it underpredicts the Ca II K line and the G band. This inadequacy can be removed once we introduce a fourth component — an intermediate-age stellar population ($1 \text{ Gyr} \leq \text{Age} \leq 3 \text{ Gyr}$, and $Z = 0.2, 0.4, 1.0$, and $2.5 Z_\odot$). Figure 6b displays the best fit four-component model, which

⁶ <http://www.strw.leidenuniv.nl/~mcappell/idl/>

⁷ Applying an additive Legendre polynomial of similar degrees led to consistent results.

⁸ At $z = 0.256$ the age of the Universe is 10.4 Gyr.

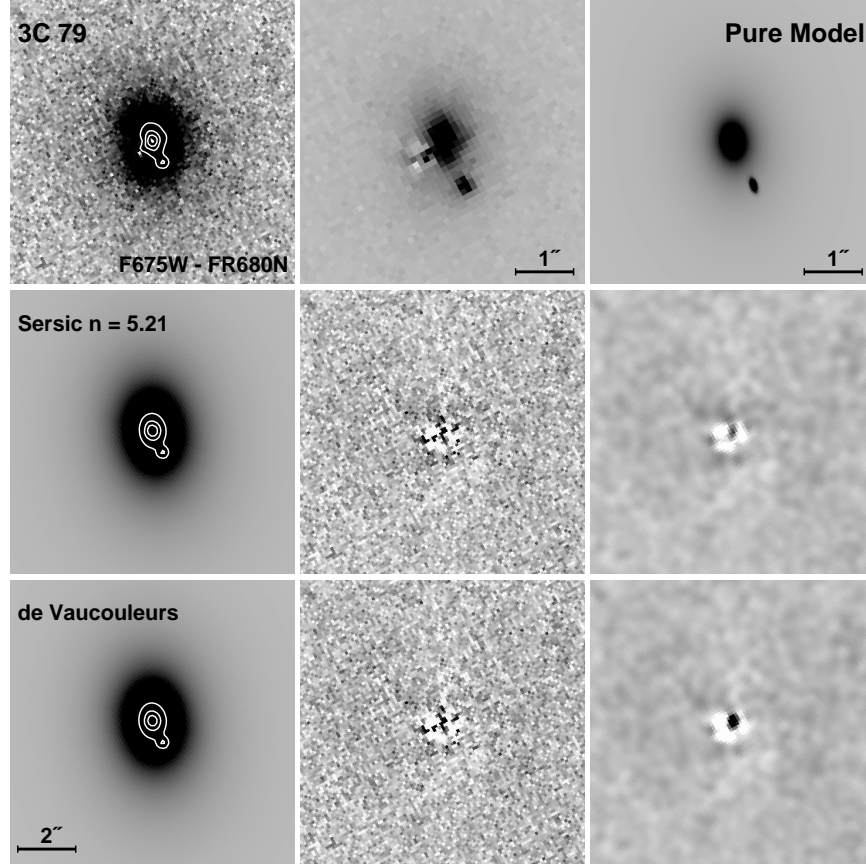


FIG. 4.— Two-dimensional modeling of 3C 79 host galaxy. The top left panel shows the WFPC2/WF emission-line free image. Directly below are best fit Sérsic and de Vaucouleurs models convolved with the PSF. The superimposed contours in these panels are from the same images but smoothed by a Gaussian function with a FWHM of 3 pixels, and are at the same levels as those in Fig. 1. To the right of each model are shown the original residual from the model subtraction and a Gaussian smoothed version. The top middle and top right panels show respectively the data and the best fit model (without convolution with the PSF), both have been magnified by a factor of two and are displayed at a lower contrast. For the companion galaxy (3C 79A), we used an exponential model and have fixed its geometric parameters ($r_{1/2}$, b/a and PA) to those obtained from modeling the WFPC2/PC1 image (see Fig. 3).

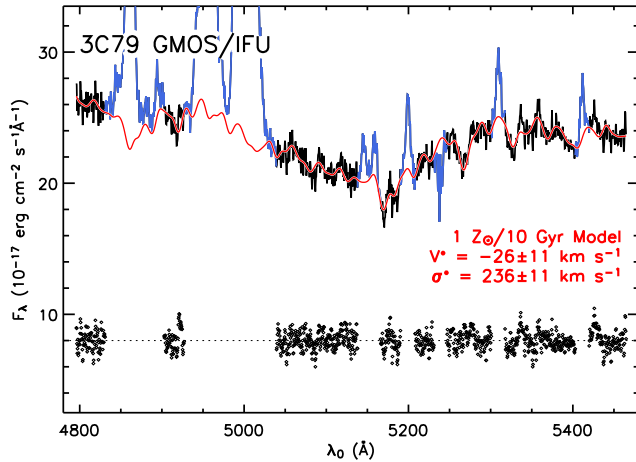


FIG. 5.— Modeling the kinematics of the central part ($r \lesssim 2$ kpc) of 3C 79 host galaxy. The GMOS/IFU rest-frame spectrum of 3C 79 host galaxy is plotted in black, with spectral regions excluded from the modeling highlighted in blue (including nuclear emission lines and a CCD chip defect). Overplotted in red is the best fit instantaneous burst model of Vazdekis (1999), with the metallicity and age labeled in red. Also labeled are the measured radial velocity of the stars relative to that of the NLR ($z = 0.25632$) and the stellar velocity dispersion. The residual after being offset by 8×10^{-17} erg cm $^{-2}$ s $^{-1}$ Å $^{-1}$ is shown with diamonds, and the dotted line going through the residual indicates the zero level.

successfully reproduces the Ca II K line and the G band ab-

sorption. The global best fit to the data is given by stellar population models with a metallicity of $2.5 Z_{\odot}$. In order to gauge how robust this metallicity result is, we compared the best fit four-component models of different metallicities. The best fit $1.0 Z_{\odot}$ model gives a generally good fit to both the absorption features and the overall continuum shape, except that it cannot reproduce the high S/N continuum shape around the Mg I b feature between 5000 and 5500 Å (rest-frame), resulting in a 16% increase in the χ^2 value relative to the $2.5 Z_{\odot}$ model. Models with sub-solar metallicities all fail to give an adequate fit, especially in the continuum below 4300 Å (rest-frame). We thus conclude that the stellar population in the host galaxy has a super-solar metallicity. A conservative range of metallicities that can give an adequate fit to the LRIS spectrum is between 1 and $2.5 Z_{\odot}$.

We have also attempted to use a young stellar population (< 0.1 Gyr) to replace the power law component, but the best fit model underpredicts the higher ($\geq H7$) Balmer lines if it correctly predicts the H γ flux (due to the Balmer absorption lines from the young population), and it gives a much poorer fit to the rest-frame UV continuum ($2900\text{Å} < \lambda_0 < 3800\text{Å}$), in particular, it overpredicts the Balmer limit break at 3650 Å.

If we adopt the average total stellar mass from the two best fit models shown in Fig. 6, then the stellar mass inside $r_{1/2}$ is $M_{1/2}^* = 2.6 \times 10^{11} M_{\odot}$. The $M_{1/2}^*/M_{1/2}^{\text{vir}}$ ratio implies a dark matter fraction of $\sim 34\%$ within one effective radius, in agree-

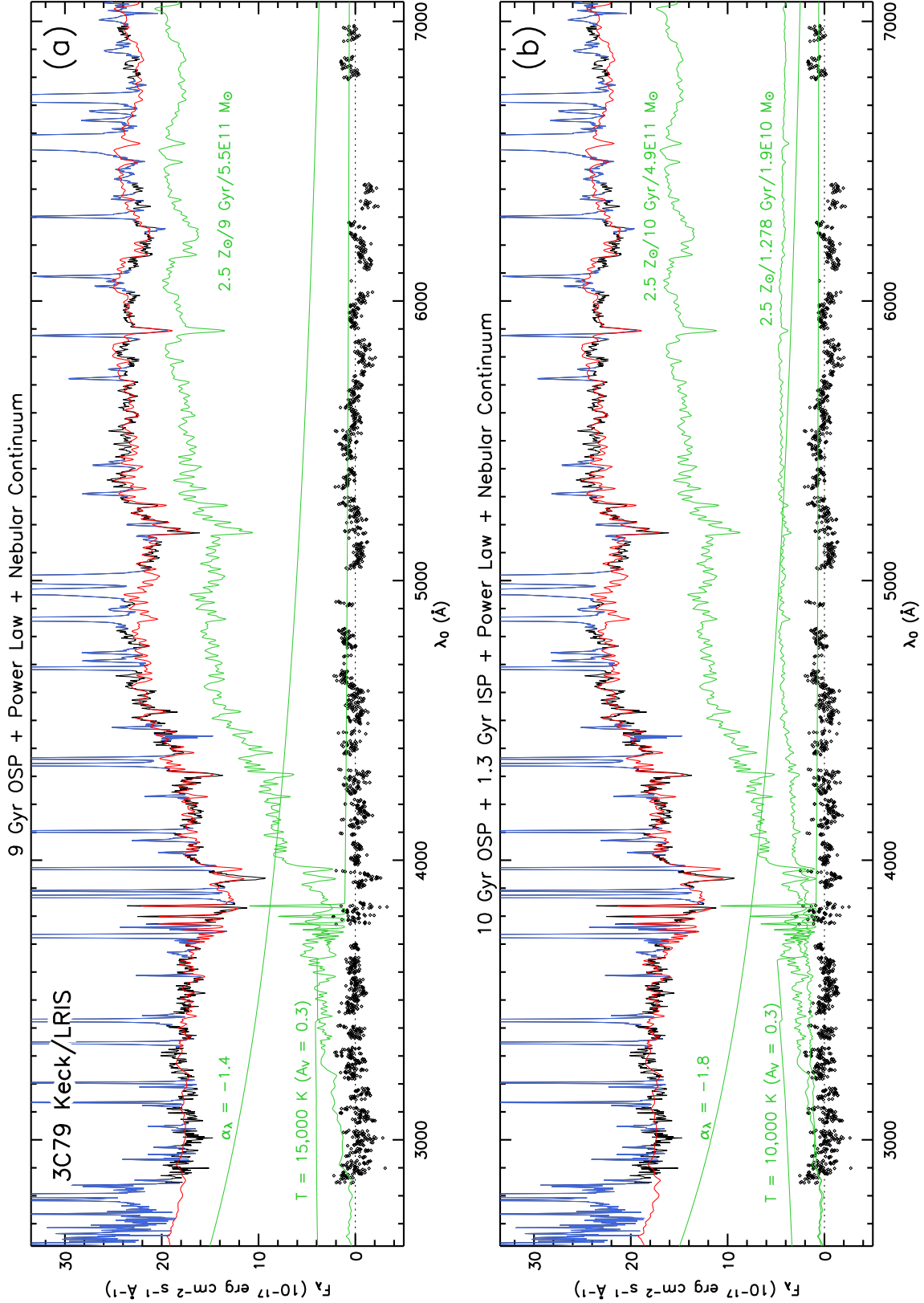


FIG. 6.— Decomposing the nuclear continuum of the 3C 79 host galaxy: (a) the best fit three-component model, and (b) the best fit four-component model. Spectral regions that were excluded from the modeling (nuclear emission lines and imperfect sky subtraction regions) are highlighted in blue. Overplotted below (green) are Bruzual & Charlot (2003) stellar population models, λ^α power laws representing quasar scattered light, and reddened nebular continua (including Balmer lines $\geq H7$). The sum of the models (red) provides the best fit to the observed spectrum. Labeled are the metallicity, age and stellar mass for the stellar population models, the temperature of the nebular continuum models and the index of the power laws. The residual is shown with diamonds, and the dotted line going through the residual indicates the zero level.

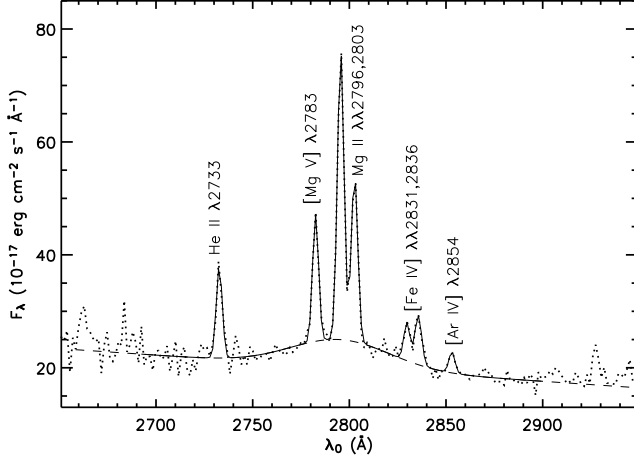


FIG. 7.— Detection of a broad Mg II $\lambda 2798$ line in the nuclear spectrum of 3C 79. Dotted curve shows the LRIS spectrum, the solid curve is a best fit model of eight Gaussians plus a linear continuum, and the long dashed curve shows the broad (FWHM ~ 6500 km s $^{-1}$) Gaussian profile of the Mg II line. Key narrow emission lines are labeled.

ment with the dark matter fraction of nearby early-type galaxies (Cappellari et al. 2006). We caution that there are significant uncertainties in both the stellar mass derived from single-burst stellar synthesis models and the dynamical mass using the virial theorem. Hence, this straightforward calculation of dark matter content is subject to an error of at least a factor of two. We note that the absolute R -band magnitude⁹ of the galaxy is about -23.2 , which is the same as that of the host galaxies of EELR quasars (Fu & Stockton 2007a).

The compact companion galaxy 3C 79A is detected in the GMOS data cube. The comparison of the spectrum extracted from 3C 79A and a background spectrum from a symmetric location with respect to the minor axis of the host galaxy shows a red continuum¹⁰, indicating an old stellar population for 3C 79A. This galaxy is reminiscent of the close companion galaxy 1'' away from the EELR quasar 3C 48 (Stockton et al. 2007), which is also elongated towards the AGN nucleus. The S/N ratio of the spectrum does not allow a detailed modeling.

4. THE EXTENDED EMISSION-LINE REGION

The *HST* LRF [O III] image (Fig. 1) shows not only the filament seen in the H α image of McCarthy et al. (1995), but also luminous emission-line “arms” at distances around 2.''5 from the nucleus, and an “inner arc” 1'' to the west. To compare the EELR of 3C 79 with those around quasars, we determined the total luminosity in the [O III] $\lambda 5007$ line within an annulus of inner radius 11.2 kpc and outer radius 44.9 kpc¹¹ ($L_{[\text{O III}]}$). We found a luminosity of $L_{[\text{O III}]} = 7.8 \times 10^{42}$ erg s $^{-1}$, close to that of the most luminous quasar EELR at $z < 0.5$, i.e., that of 4C 37.43, $L_{[\text{O III}]} = 9.4 \times 10^{42}$ erg s $^{-1}$ (converted from Stockton & MacKenty 1987). As a reference, the least luminous detected EELR in the radio-loud quasar subsample of Stockton & MacKenty (1987) has a luminosity about 10 times lower (PKS 2135–147, $L_{[\text{O III}]} = 6.9 \times 10^{41}$ erg s $^{-1}$).

⁹ Converted from the F675W ST system to R -band Vega system (-0.7 mag), after applying k -correction (-0.27) and passive evolution correction ($+0.23$), following Labita et al. (2006).

¹⁰ The continuum shape did not change much after we corrected it for the “fixed-aperture effect” (Fu & Stockton 2007b).

¹¹ This is equivalent to the 10 kpc/40 kpc annulus used by Stockton & MacKenty (1987) since they assumed an empty universe with $H_0 = 75$ km s $^{-1}$ Mpc $^{-1}$ and $q_0 = 0$.

4.1. Gas Kinematics

Kinematics of the ionized gas can be measured from strong emission lines. Since a single 48 min GMOS exposure is enough to acquire a good S/N ratio in the [O III] $\lambda 5007$ line region, we derived the velocity fields from the single data cube that has the smallest airmass (AM = 1.172) and the best seeing. To study the velocity structure for the clouds in the inner arc that is only 1'' from the nuclear NLR, we subtracted the light from the NLR and the bright nearby cloud 0.''5 east to the NLR by simultaneously fitting two Moffat PSF profiles at each wavelength in the wavelength range where both clouds are apparent¹². After trials it was found that the best subtraction results came from using the best fit Moffat profile from modeling the Feige 34 data cube over the same wavelength range, indicating both data cubes have the same resolution (FWHM $\simeq 0.''6$ at the [O III] region). We then fixed the Moffat parameters to those of the standard star and let the positions and magnitudes vary. Finally, we fixed the positions to the average values across the wavelength range from the previous fit and performed the fit with only the magnitudes as free parameters. The resulting PSF-subtracted data cube is presented as a set of velocity channel maps in Fig. 8. The velocity field is shown in Fig. 9. The velocity dispersion measurements have been corrected for the $\sigma_0 = 42$ km s $^{-1}$ instrumental resolution. Due to the imperfect PSF subtraction process, no useful kinematics can be extracted from the PSF-subtracted data cube in the nuclear region bordered by the white no-data pixels in Fig. 9. Hence, we measured the velocity field in this region from the original data cube and inserted the results into the final velocity field.

Most of the extended emission comes from two main filaments — the inner arc and the outer arm 2.''5 from the nucleus. Both filaments show similar velocity gradients, with the northern part approaching towards us and the southern part receding from us at velocities of ~ 200 km s $^{-1}$. Together, these two filaments are consistent with a common disk rotation with a flat rotation curve. This sort of locally ordered kinematics of the brighter clouds is reminiscent of that of the three most luminous clouds southeast of 3C 249.1 (Fu & Stockton 2006). However, the much fainter clouds outside of the outer arc disrupt this simple picture by showing large approaching velocities.

The velocity dispersion over most of the region is around 50 to 120 km s $^{-1}$. The region showing large σ (150–200 km s $^{-1}$) between the inner arc and the outer arm, although roughly coincident with the jet direction, in fact also has multiple velocity components that happen to contribute light to the same pixels.

Overall, the velocity field of the 3C 79 EELR is similar to those of the quasar EELRs, in the sense that all of them appear globally disordered but locally ordered, and they all show super-sonic velocity dispersions (sound speed $c_s \sim 17$ km s $^{-1}$) within the same range between 50 and 130 km s $^{-1}$ (Fu & Stockton 2006, 2007b).

4.2. Spectra of Emission-Line Clouds

To increase the S/N ratio, we have combined GMOS spectra within various regions. The spectra of the clouds in the inner arc ($r \leq 1.''2$) are heavily contaminated by light from the nuclear NLR, making it difficult to measure their line intensities accurately. We therefore concentrated on the EELR

¹² The two clouds have essentially the same velocity, at $z = 0.25632 \pm 0.00001$.

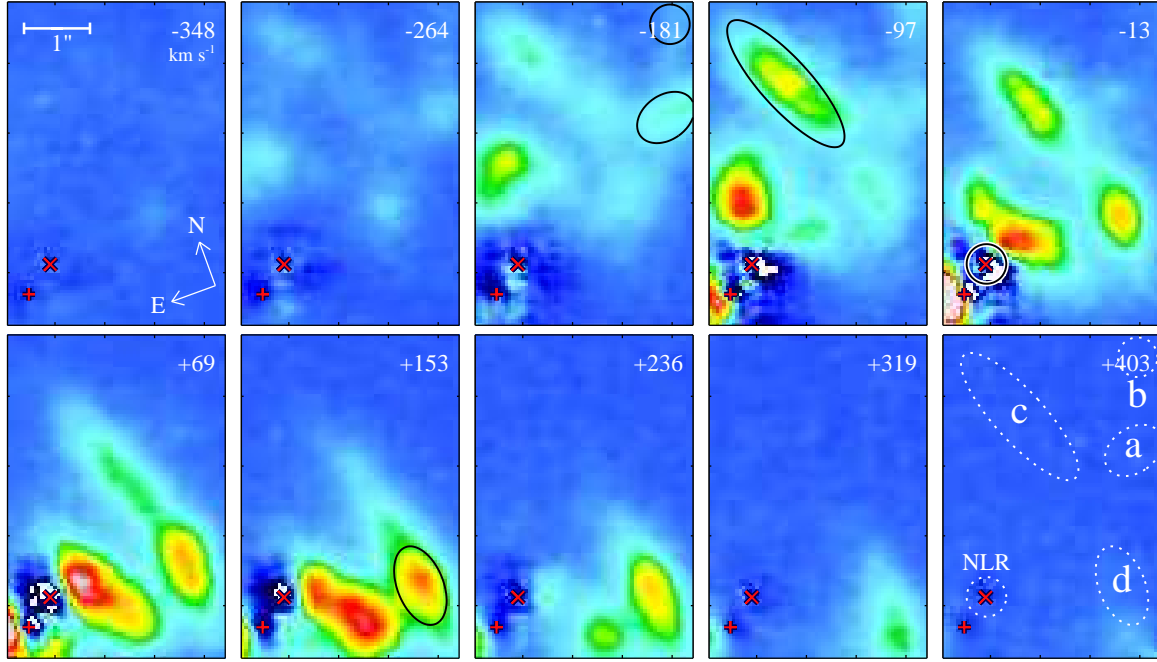


FIG. 8.— GMOS/IFU [O III] $\lambda 5007$ radial velocity channel maps for the 3C 79 EELR. The central velocities, in km s^{-1} , relative to that of the quasar NLR, are indicated in the upper right corner of each panel. The red multiplication signs mark the nuclear narrow-line region, and the red plus signs indicate the brightest nearby emission-line cloud, both of which have been subtracted from the data cube to show the EELR more clearly. Solid ellipses show the extraction apertures of the five emission-line clouds discussed in § 4.2 in individual panels corresponding to their central velocities. In the last panel these apertures are shown all together as dashed ellipses, along with their names labeled nearby.

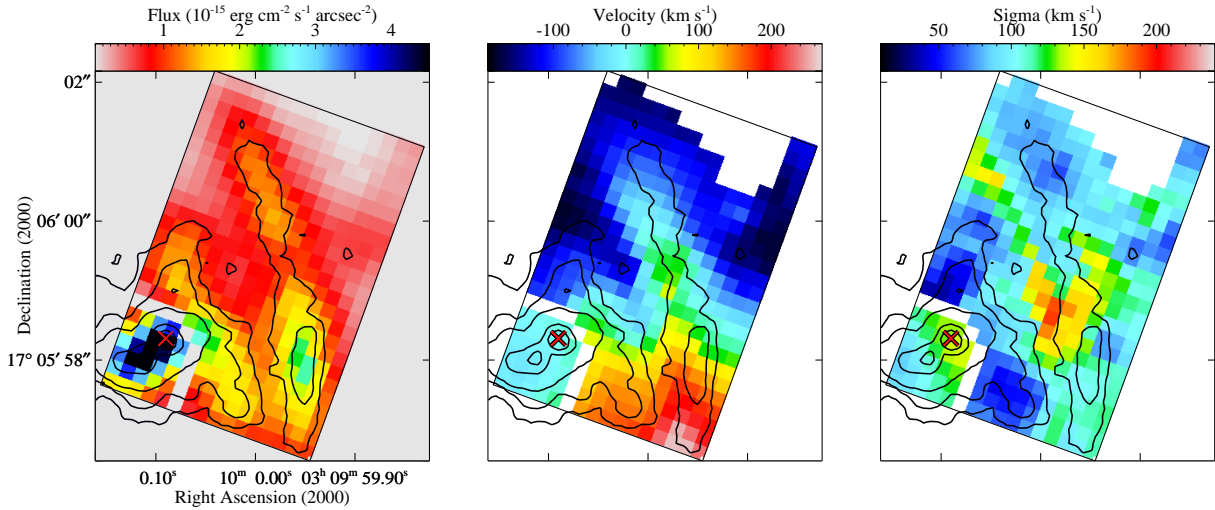


FIG. 9.— GMOS/IFU [O III] $\lambda 5007$ velocity field of the 3C 79 EELR. Inside the FOV there is a white no-data boundary near the nuclear region. The velocity field outside of the boundary is measured from a data cube where both the nuclear NLR and the bright emission-line cloud directly to the east were removed (see also Fig. 8), while inside the boundary the data come from the original data cube. The fluxes inside the boundary were scaled down by a factor of 6 to show the high surface brightness peaks. Overlaid are contours from the *HST* WF3 LRF [O III] image smoothed by a Gaussian function with a FWHM of 1.5 pixels; contours are at levels of $1.8 \times 10^{-15} \times (1, 2, 4, 20, 40) \text{ erg cm}^{-2} \text{ s}^{-1} \text{ arcsec}^{-2}$. The three panels, from left to right, are line intensity, radial velocity (relative to that of the nuclear NLR) and velocity dispersion maps. Pixels are $0''.2$ squares. The red multiplication signs indicate the center of the host galaxy.

clouds in the outer arm and beyond. In Fig. 8 we have shown the extraction apertures for the four EELR clouds. We have also extracted a NLR spectrum using a circular aperture with a radius of $0''.3$. In order to measure the key metallicity diagnostic — the $[\text{N II}] \lambda 6584/\text{H}\alpha$ ratio — we extracted LRIS spectra from three regions along the slit: a $2''$ -wide aperture centered on the nucleus was used for the nuclear NLR, and the apertures used for the *N1* and *S1* regions are shown in Fig. 1.

Unlike those for the EELR clouds, NLR spectra should be corrected for stellar absorption features. We fitted the continuum using the same stellar synthesis model templates as in § 3.3 and subtracted off the best fit model to obtain the clean emission-line spectrum of the NLR. Note that the line ratios for the NLR should be reliable even if the continuum subtraction were just barely correct, given the large equivalent widths of the emission lines that are affected by strong

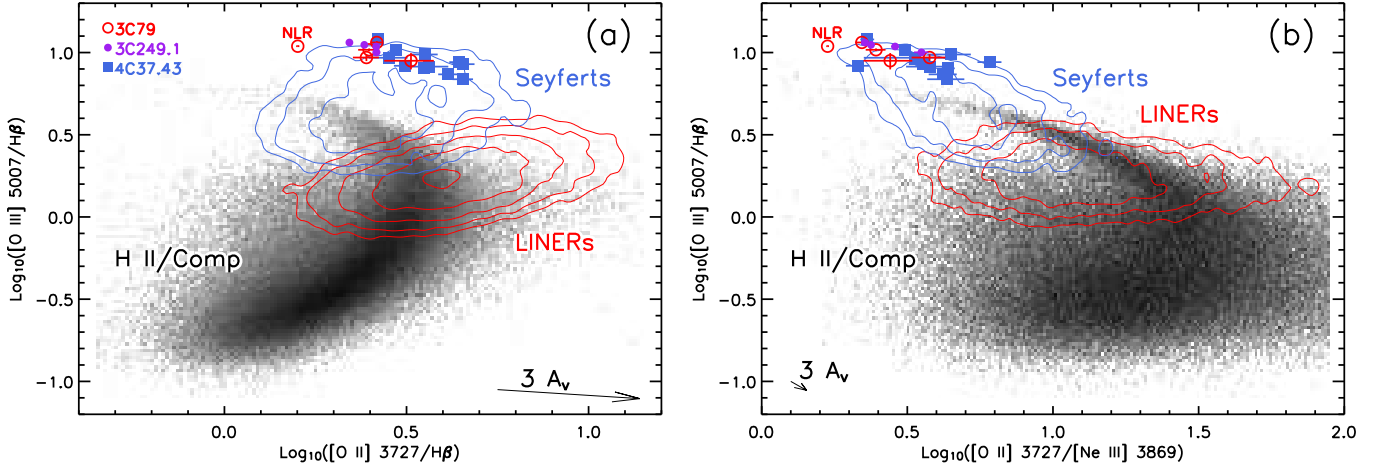


FIG. 10.— Log-scaled density distributions of SDSS Seyferts (blue contours), LINERs (red contours), and star-forming galaxies (including starburst-AGN composite galaxies; the background image) in line-ratio diagrams: (a) $[\text{O II}] \lambda\lambda 3726, 3729/\text{H}\beta$ vs. $[\text{O III}] \lambda 5007/\text{H}\beta$, and (b) $[\text{O II}] \lambda\lambda 3726, 3729/[\text{Ne III}] \lambda 3869$ vs. $[\text{O III}] \lambda 5007/\text{H}\beta$. Measurements from the EELRs of 3C 79, 3C 249.1, and 4C 37.43 are shown as red open circles, violet solid circles and blue squares, respectively (Fu & Stockton 2006, 2007b). Both diagrams clearly show that the EELRs are photoionized by an AGN-type ionizing spectrum.

absorption features. Intrinsic reddening due to dust in front of or associated with the cloud was determined from the measured $\text{H}\gamma/\text{H}\beta$ ratio for GMOS spectra and from $\text{H}\alpha/\text{H}\beta$ ratio for LRIS spectra, assuming theoretical ratios of 0.468 for $\text{H}\gamma/\text{H}\beta$ (the value for case B recombination at $T = 10^4$ K and $N_e = 10^2 \text{ cm}^{-3}$; Osterbrock 1989) and 3.1 for $\text{H}\alpha/\text{H}\beta$. For clouds *a* and *b*, where the S/N ratio of the $\text{H}\gamma$ line is poor, we assumed zero intrinsic reddening. For clouds *N1* and *S1*, where the measured $\text{H}\alpha/\text{H}\beta$ is slightly lower than the theoretical value, we also assumed zero intrinsic reddening. Both the intrinsic reddening and Galactic reddening were corrected using a standard Galactic reddening law (Cardelli et al. 1989).

The reddening-free emission-line fluxes and 3σ upper limits are tabulated in Table 2. The quoted 1σ errors were derived from the covariance matrices associated with the Gaussian model fits, with the noise level estimated from line-free regions on either side of an emission line.

There is enough overlapping area to show that the data from the two instruments agree fairly well: (1) The low intrinsic reddening for cloud *c* is consistent with the measured $\text{H}\alpha/\text{H}\beta$ ratio of 3.09 in region *N1*; (2) The GMOS NLR spectrum suggests an intrinsic reddening of $A_V = 0.28$, whilst the LRIS NLR spectrum shows $A_V = 0.36$; (3) The individual line ratios relative to $\text{H}\beta$ of regions *c* and NLR (GMOS) are very much consistent with those measured from the LRIS *N1* and NLR spectra, respectively.

4.2.1. Electron Density and Temperature

The $[\text{O II}]$ luminosity-weighted average electron density (N_e) and electron temperature (T_e) can be measured from the intensity ratio of the $[\text{O II}] \lambda\lambda 3726, 3729$ doublet and the $[\text{O III}] (\lambda 4959 + \lambda 5007)/\lambda 4363$ ratio, respectively (Osterbrock 1989). Our GMOS data cube covers all of these five lines, allowing us to measure the density and temperature in individual emission-line clouds. The $[\text{S II}] \lambda\lambda 6717, 6731$ doublet is covered by the LRIS spectra, however, they fall into the region where strong OH night sky lines dominate and severe CCD fringing occurs, preventing reliable measurements. We thus only discuss results from the $[\text{O II}]$ doublet.

The $[\text{O II}]$ doublet is barely resolved in our spectra. However, for the NLR and the EELR clouds *c* & *d*, the high S/N ratio profile of the doublet allows a meaningful decomposition once we constrain their expected wavelengths to be at the

same redshift as that of the nearby $[\text{Ne III}] \lambda 3869$ line. Uncertainties of the line fluxes from this fit tend to be low as the wavelengths are no longer free parameters. Lifting this wavelength constraint gives a more conservative error estimate. Here we have adopted the mean values of the error estimates from the two fits — one with and one without wavelength constraints. The weak $[\text{O III}] \lambda 4363$ line is detected in all the clouds except *b*. We then derived T_e and N_e consistently using the IRAF routine TEMDEN for the three regions where both $[\text{O II}]$ and $[\text{O III}]$ ratios are available. Table 3 summarizes the results. For the clouds in the EELR, the temperatures are about 12,000 to 14,000 K, and the densities are about $100\text{--}200 \text{ cm}^{-3}$, similar to those of quasar EELRs that were measured using the same technique (Stockton et al. 2002; Fu & Stockton 2006, 2007b).

4.2.2. Ionization Mechanisms

The emission-line ratios of the 3C 79 clouds are very similar to those of the quasar EELRs. Previously we have concluded that the spectra of quasar EELRs are most consistent with being photoionized by quasar continuum, and are inconsistent with shock or the self-ionizing “shock + precursor” models (Fu & Stockton 2007b). Now we re-emphasize this point by comparing strong line ratios of the EELRs of the radio galaxy 3C 79 and the quasars 3C 249.1 and 4C 37.43 with emission-line galaxies at a similar redshift range. The Sloan Digital Sky Survey Data Release 4 (SDSS DR4) provides high-quality optical spectra for a large number of galaxies. The emission-line fluxes after correcting for stellar absorption and foreground extinction are publicly available¹³. We first created a subsample of SDSS emission-line galaxies by including only those with $\text{S/N} > 3$ in the strong emission-lines $[\text{O II}] \lambda 3727 (= \lambda 3726 + \lambda 3729)$, $\text{H}\beta$, $[\text{O III}] \lambda 5007$, $\text{H}\alpha$, $[\text{N II}] \lambda 6584$ and $[\text{S II}] \lambda\lambda 6717, 6731$. Then we divided the sample into star-forming galaxies and AGN using the empirical dividing line of Kauffmann et al. (2003), and corrected for the intrinsic reddening using the Balmer decrement and the standard Galactic reddening curve (Cardelli et al. 1989). The theoretical values for the $\text{H}\alpha/\text{H}\beta$ ratio are 2.85 for star-forming galaxies and 3.1 for AGN. Finally, we classified

¹³ <http://www.mpa-garching.mpg.de/SDSS/DR4/>; and see Tremonti et al. (2004) for a description of the data.

the galaxies into Seyferts, LINERs, star-forming galaxies and AGN/starforming composites, following the classification schemes of Kewley et al. (2006).

Figure 10 compares the locations of our EELRs and the distributions of the SDSS galaxies in two line-ratio diagnostic diagrams. As can be seen, the EELRs share the same territory as the Seyfert galaxies, but are clearly distinguishable from star-forming and composite galaxies, indicating that the EELRs are photoionized by an AGN-type ionizing spectrum.

The line-ratios from the 3C 79 EELR match those from 3C 249.1 and 4C 37.43 very well, thus pure shock and “shock + precursor” models can be ruled out, since it has been shown (using the same line-ratios) that these models do not fit these quasar EELRs (see Fig. 5 of Fu & Stockton 2007b for an example).

4.2.3. Gas Metallicity

With the knowledge that the EELR of 3C 79 is photoionized by the hidden quasar, we can now estimate the metallicity of the gas using photoionization models. In the following we will compare our data with the dusty radiation-pressure dominated photoionization models of Groves et al. (2004) with a density of 1000 cm^{-3} . Since the diagnostic line ratios we will use are almost entirely dependent on the abundances, models adopting a different density will not change our results.

As the metallicity of a photoionized nebula increases, the temperature of the nebula decreases (as a result of the increased metal cooling), and the relative strengths between hydrogen lines and lines from other heavier elements also decreases (due to the increased abundance of the heavy elements relative to hydrogen). The latter effect is especially strong for nitrogen lines since the element is dominated by “secondary” production¹⁴ at $Z \gtrsim 0.2 Z_{\odot}$. Hence, N abundance increases at a much faster rate with metallicity, i.e., $N/H \propto Z^2$. In Figure 11a we use the temperature sensitive $[O III] \lambda 4363/\lambda 5007$ ratio to demonstrate the dependance of nebula temperature on metallicity. The stratification among the grids of different metallicities is further improved by the fact that helium increases linearly with metallicity relative to hydrogen (Pagel et al. 1992). In Fig. 11b and Fig. 12, we show the strong dependance of $[N I] \lambda 5199/H\beta$ and $[N II] \lambda 6584/H\alpha$ on metallicity. At each metallicity, we show models spanning a range of ionization parameters ($-2.3 \leq \log(U) \leq 0$) and four power-law indices from $\alpha = -1.2$ to -2.0 , representing the quasar ionizing continuum ($F_{\nu} \propto \nu^{\alpha}$). We have converted the modeled total metallicities to gas-phase metallicities using the solar abundances defined by Anders & Grevesse (1989) ($12 + \log(O/H)_{\odot} = 8.93$ and $Z_{\odot} = 0.02$), in order to be consistent with both previous studies on the metallicity of quasar BLRs and metallicity results from stellar populations (§ 3.3). One solar metallicity in Groves et al. (2004) corresponds to $1/3 Z_{\odot}$ in our figures, since approximately half of the metals are assumed to be depleted onto dust in the models, and their assumed solar metallicity is about 0.2 dex¹⁵ lower than that of Anders & Grevesse (1989).

As can be seen in Figs. 11 & 12, the line-ratios of the EELR as well as the NLR of 3C 79, like those quasar EELRs and their BLRs, are most consistent with a low-metallicity

at about $1/3$ to $2/3$ solar. Fig. 12 illustrates the peculiarity of 3C 79 more clearly by comparing it directly with SDSS AGN on the same line-ratio diagnostic. The nuclear NLR along with the two other regions where we have $[N II]$ measurements all lie on the lower metallicity side of the main Seyfert branch, overlapping with quasar EELRs. This result supports the orientation-based unification schemes of FR II radio galaxies and radio-loud quasars (Barthel 1989). On the other hand, 3C 79 offers yet another example strengthening (1) the correlation between the presence of EELRs and the metallicity of the nuclear gas (BLRs and/or NLRs), and (2) the similar metallicity in EELRs and the gas in the nuclear region. Both correlations were initially discovered only among steep-spectrum radio-loud quasars (Fu & Stockton 2007a).

5. DISCUSSION

5.1. The Origin of the Low-Metallicity Gas

The great majority of quasars show super-solar metallicities in their nuclear regions (see Hamann et al. 2007, for a recent review); yet, as we have previously shown (Fu & Stockton 2007a), quasars with luminous EELRs are drawn exclusively from the subset of steep-radio-spectrum quasars that have BLRs with sub-solar metallicities. The fact that the quasar host galaxies are almost always very massive and thus expected to have high metallicities suggests an external source for the low-metallicity gas. Furthermore, the apparent link between the metallicity of the gas in the BLRs and the metallicity of the gas in the EELRs, which have minimum masses of $10^{9-10} M_{\odot}$, means that the external source of the gas must itself have been moderately massive.

In 3C 79, we have an FR II radio galaxy that shows the same pattern. Although we of course cannot obtain a broad-line-region metallicity in this case, we have used the unresolved nuclear narrow-line region metallicity as a surrogate. Aside from providing a consistency check on unified models for FR II radio galaxies and quasars, the main question of interest is whether the clearer view of the inner region of the host galaxy gives us any insight into the origin of the low-metallicity gas and the mechanism that produced the EELR.

The host galaxy of 3C 79 appears to be a fairly normal elliptical morphologically. The most intriguing feature in the inner region is the extremely compact galaxy $0''.8$ from the center of the host galaxy. The nearly exponential profile of this galaxy suggests that it could be a tidally stripped “pseudobulge” of a late-type galaxy (e.g., Kormendy & Kennicutt 2004); the interstellar medium of such a galaxy would be quite plausible as a source for the low-metallicity gas in 3C 79. We have suggested elsewhere (Stockton et al. 2007; Fu & Stockton 2007b) that luminous EELRs may result from nearly spherical blast waves connected with the initiation of FR II radio jets. The connection with low-metallicity gas is less clear, although we can speculate that it may have something to do with the lower radiative coupling such gas would have to the quasar radiation field, allowing more efficient accretion. It is interesting to note that related considerations have been invoked recently to explain the link between low metallicity and long-duration gamma-ray bursts (Fruchter et al. 2006) on the scale of massive stars, although the physical mechanisms involved are certainly different.

5.2. Low-Metallicity Radio Galaxies in SDSS

Armed with the latest photoionization models, Groves et al. (2006) identified ~ 40 (out of ~ 23000) candidates of low-metallicity Seyfert2s in SDSS. A caveat to note is that

¹⁴ where nitrogen is synthesized from existing carbon and oxygen (Pagel & Edmunds 1981).

¹⁵ The C, N, O, and Fe abundances in the solar abundance set assumed by Groves et al. (2004) are all ~ 0.2 dex lower than those in Anders & Grevesse (1989). Hence, the mass fraction of metals (i.e. Z) is about 1.5 times lower — $Z_{\odot} = 0.013$ — than that of Anders & Grevesse (1989).

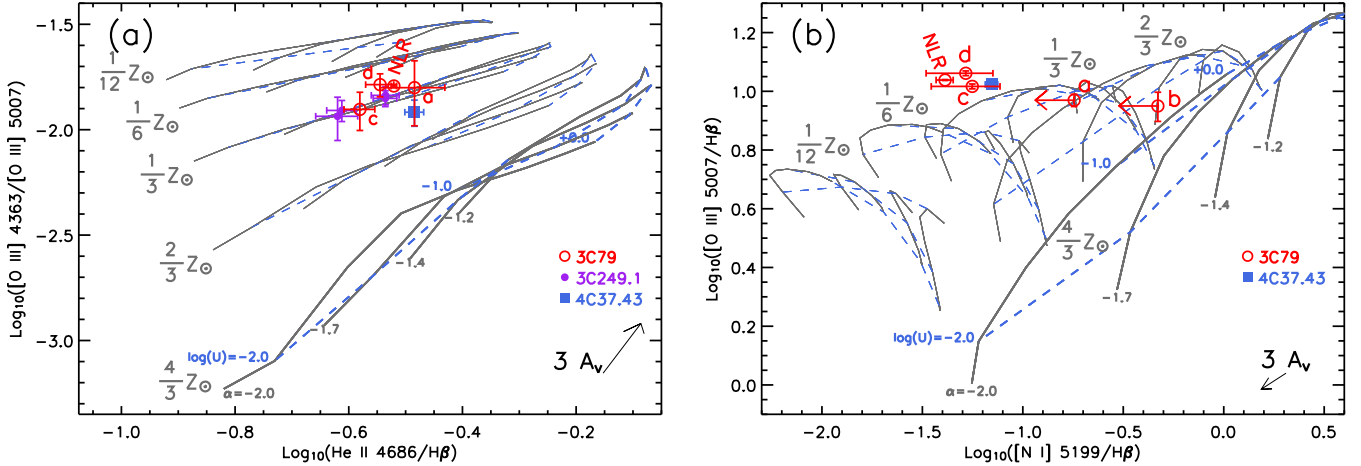


FIG. 11.— Metallicity-sensitive line-ratio diagrams: (a) $\text{He II } \lambda 4686/\text{H}\beta$ vs. $[\text{O III}] \lambda 4363/[\text{O III}] \lambda 5007$, and (b) $[\text{N I}] \lambda 5199/\text{H}\beta$ vs. $[\text{O III}] \lambda 5007/\text{H}\beta$. Measurements from the EELRs of 3C 79, 3C 249.1, and 4C 37.43 are shown as red open circles, violet solid circles and blue squares, respectively (Fu & Stockton 2006, 2007b). Besides 3C 79, accurate $[\text{N I}]$ flux measurements are only available for 4C 37.43 E1 (Stockton et al. 2002). Photoionization model grids from Groves et al. (2004) are shown for five metallicities from 0.1 to $1.3 Z_{\odot}$. For each metallicity, model predictions are given for a range of ionization parameters ($-2.3 \leq \log(U) \leq 0$) and four power law indices representing the quasar ionizing continuum ($F_{\nu} \propto \nu^{\alpha_{\nu}}$; $\alpha_{\nu} = -1.2, -1.4, -1.7$, and -2.0). The grids for the highest metallicity are highlighted to show the inconsistency between our data and predictions assuming super-Solar metallicity gas. Both diagrams show that the EELR of 3C 79 consists of sub-solar metallicity gas, matching the gas metallicity of the EELRs of 3C 249.1 and 4C 37.43 (Fu & Stockton 2007b), as well as the metallicity of the BLRs of radio-loud quasars showing EELRs (Fu & Stockton 2007a).

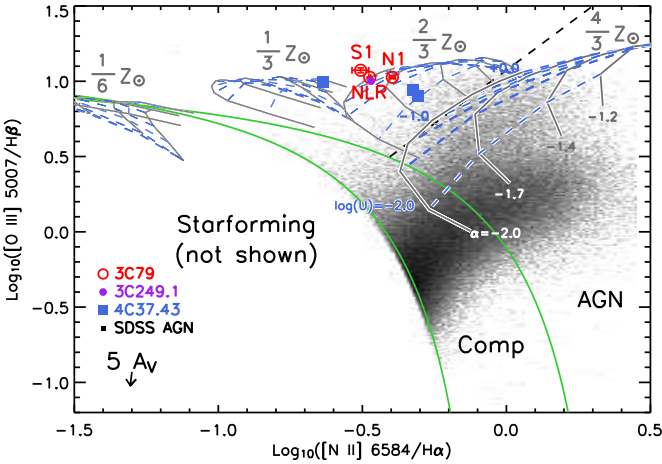


FIG. 12.— The nuclear NLR and EELR of 3C 79, along with quasar EELRs, are much metal-poorer than in typical AGN, as seen in the metallicity diagnostic diagram of $[\text{N II}] \lambda 6584/\text{H}\alpha$ vs. $[\text{O III}] \lambda 5007/\text{H}\beta$. Keys are the same as in Fig. 11. The background image shows the density distribution of the SDSS AGN sample in log scale. Objects above the upper green curve are objects dominated by AGN (LINERs are concentrated in the lower denser branch and Seyferts in the upper branch; Kewley et al. 2006), below the lower curve are starforming galaxies (Kauffmann et al. 2003), and AGN/starforming composite galaxies are in between. Most Seyferts can be fit quite well with the super-solar metallicity models. The top region bordered by the black dashed line and the upper green curve is where the low-metallicity Seyferts are located (Groves et al. 2006).

the authors restricted the sample to galaxies with stellar masses lower than $10^{10} M_{\odot}$ while selecting their candidates, as guided by the mass-metallicity correlation (e.g. Tremonti et al. 2004). Although the EELR quasars are excluded from the SDSS emission-line galaxy sample, 3C 79 represents a population of low-metallicity AGN that were missed by Groves et al. These AGN are hosted by massive evolved galaxies with $\sim 10^{12} M_{\odot}$ of stars and harbor $\sim 10^9 M_{\odot}$ black holes at their hearts, and they are likely to be more powerful than the Seyfert2s.

By cross-correlating the TEXAS radio galaxies (Douglas et al. 1996) with SDSS DR4 AGN, we have identified a sample of low-metallicity radio galaxies. Like

that of 3C 79, the spectra of their host galaxies show red slopes and absorption features that are indicative of an old stellar population. Follow-up high-resolution imaging and spatially resolved spectroscopy of these galaxies and a comparable control sample are needed to finally nail down the source of the low-metallicity gas and the triggering mechanism for quasar superwinds. In addition, detecting EELRs around these objects would provide a new test for the unification schemes.

6. SUMMARY

Based on extensive ground-based spectroscopy and archival *HST* WFPC2 images of the radio galaxy 3C 79, we have conducted a detailed analysis of its host galaxy and the EELR. The host galaxy of 3C 79 is a massive elliptical with $M_R = -23.2$. The UV/optical spectral energy distribution of the host galaxy is best described by a combination of an intermediate-age stellar population (1.3 Gyr), an old stellar population (10 Gyr), a power law, and a nebular thermal continuum. Both stellar populations are metal rich ($2.5 Z_{\odot}$). This best fit model indicates a total stellar mass within one effective radius of approximately $2.5 \times 10^{11} M_{\odot}$, consistent with the virial mass derived from stellar kinematics ($\sim 4 \times 10^{11} M_{\odot}$).

The EELR of 3C 79 is remarkably similar to the most luminous quasar EELRs. The velocity field, although only available in a small area, is locally ordered but globally disordered. The EELR is almost certainly photoionized by the hidden quasar, and it shows densities of $\sim 100 \text{ cm}^{-3}$ in the $[\text{O II}]$ emitting regions and temperatures around 13,000 K. Most interestingly, the metallicity of the gas in both the EELR and the NLR is about $1/3$ – $2/3$ solar, matching perfectly the metallicity in both the EELRs and the nuclear BLRs of the EELR quasars.

There is a very compact close companion galaxy 3.3 kpc from and 4 magnitudes fainter than the host galaxy. This companion galaxy shows an exponential profile, and is presumably a tidally stripped “pseudobulge” of a late-type galaxy that might be the source for the low-metallicity gas as well as the starforming regions in 3C 79.

The exact correspondence between this EELR and the

EELRs around quasars joins the already overwhelming evidence in support of the unification schemes for FR II radio galaxies and radio-loud quasars. The definitive trait of sub-solar metallicity in the NLR of 3C 79 also provides an efficient tool for selecting FR II radio galaxies that likely host luminous EELRs.

We thank the Gemini staff for carrying out the GMOS observations and Nicola Bennert for helping us obtain the LRIS spectra. We also thank the anonymous referee for a careful reading of the manuscript and for cogent comments to help us clarify and improve the presentation. This research has been partially supported by NSF grant AST03-07335.

REFERENCES

- Allington-Smith, J., et al. 2002, *PASP*, 114, 892
 Anders, E., & Grevesse, N. 1989, *Geochimica et Cosmochimica Acta*, 53, 197
 Antonucci, R., Hurt, T., & Kinney, A. 1994, *Nature*, 371
 Barthel, P. D. 1989, *ApJ*, 336, 606
 Boroson, T. A., & Oke, J. B. 1984, *ApJ*, 281, 535
 —. 1987, *PASP*, 99, 809
 Bruzual, G., & Charlot, S. 2003, *MNRAS*, 344, 1000
 Cappellari, M., et al. 2006, *MNRAS*, 366, 1126
 Cappellari, M., & Emsellem, E. 2004, *PASP*, 116, 138
 Cardelli, J. A., Clayton, G. C., & Mathis, J. S. 1989, *ApJ*, 345, 245
 de Koff, S., Baum, S. A., Sparks, W. B., Biretta, J., Golombek, D., Macchetto, F., McCarthy, P., & Miley, G. K. 1996, *ApJS*, 107
 Di Matteo, T., Springel, V., & Hernquist, L. 2005, *Nature*, 433, 604
 Douglas, J. N., Bash, F. N., Bozyan, F. A., Torrence, G. W., & Wolfe, C. 1996, *AJ*, 111
 Dunlop, J. S., McLure, R. J., Kukula, M. J., Baum, S. A., O’Dea, C. P., & Hughes, D. H. 2003, *MNRAS*, 340, 1095
 Emsellem, E., et al. 2004, *MNRAS*, 352, 721
 Fruchter, A. S., et al. 2006, *Nature*, 441, 463
 Fu, H., & Stockton, A. 2006, *ApJ*, 650, 80
 —. 2007a, *ApJ*, 664, L75
 —. 2007b, *ApJ*, 666, 794
 Groves, B. A., Dopita, M. A., & Sutherland, R. S. 2004, *ApJS*, 153, 9
 Groves, B. A., Heckman, T. M., & Kauffmann, G. 2006, *MNRAS*, 371, 1559
 Hamann, F., Warner, C., Dietrich, M., & Ferland, G. 2007, *ASP Conference Series*, in press (arXiv:astro-ph/0701503)
 Hardcastle, M. J., Alexander, P., Pooley, G. G., & Riley, J. M. 1997, *MNRAS*, 288, 859
 Hes, R., Barthel, P. D., & Hoekstra, H. 1995, *A&A*, 303
 Hook, I. M., Jørgensen, I., Allington-Smith, J. R., Davies, R. L., Metcalfe, N., Murawinski, R. G., & Crampton, D. 2004, *PASP*, 116, 425
 Kauffmann, G., et al. 2003, *MNRAS*, 346, 1055
 Kewley, L. J., Groves, B., Kauffmann, G., & Heckman, T. 2006, *MNRAS*, 372, 961
 Kormendy, J., & Kennicutt, Robert C., J. 2004, *ARA&A*, 42, 603
 Labita, M., Treves, A., Falomo, R., & Uslenghi, M. 2006, *MNRAS*, 373, 551
 McCarthy, P. J., Baum, S. A., & Spinrad, H. 1996, *ApJS*, 106
 McCarthy, P. J., Spinrad, H., & van Breugel, W. 1995, *ApJS*, 99
 Miller, J. S. 1981, *PASP*, 93, 681
 Ogle, P. M., et al. 1997, *ApJ*, 482, 37
 Oke, J. B., et al. 1995, *PASP*, 107, 375
 Osterbrock, D. E. 1989, *Astrophysics of Gaseous Nebulae and Active Galactic Nuclei* (Mill Valley: University Science Books)
 Pagel, B. E. J., & Edmunds, M. G. 1981, *ARA&A*, 19, 77
 Pagel, B. E. J., Simonson, E. A., Terlevich, R. J., & Edmunds, M. G. 1992, *MNRAS*, 255, 325
 Peng, C. Y., Ho, L. C., Impey, C. D., & Rix, H.-W. 2002, *AJ*, 124, 266
 Schlegel, D. J., Finkbeiner, D. P., & Davis, M. 1998, *ApJ*, 500
 Spangler, S. R., Myers, S. T., & Pogge, J. J. 1984, *AJ*, 89, 1478
 Stockton, A., Canalizo, G., Fu, H., & Keel, W. 2007, *ApJ*, 659, 195
 Stockton, A., Fu, H., & Canalizo, G. 2006, *New Astronomy Review*, 50, 694
 Stockton, A., & MacKenty, J. W. 1987, *ApJ*, 316, 584
 Stockton, A., MacKenty, J. W., Hu, E. M., & Kim, T.-S. 2002, *ApJ*, 572, 735
 Tremonti, C. A., et al. 2004, *ApJ*, 613, 898
 van Dokkum, P. G. 2001, *PASP*, 113, 1420
 Vanden Berk, D. E., et al. 2001, *AJ*, 122, 549
 Vazdekis, A. 1999, *ApJ*, 513, 224

TABLE 1
MORPHOLOGY OF 3C 79 HOST GALAXY AND ITS CLOSE COMPANION

Galaxy	Model	F675W ^a	F702W ^a	$r_{1/2}$ /kpc	n^b	b/a	P.A.
3C79A	Sérsic	...	22.19	0.22	1.23	0.49	18.2
...	Exp	22.24	22.23	0.22	(1)	0.48	18.0
3C79	Sérsic	18.06	...	10.1	5.21	0.70	6.2
...	de Vauc	18.24	...	7.2	(4)	0.71	5.7
Dunlop ^c	de Vauc	17.46	...	7.5	(4)	1.0	13

^a ST magnitudes corrected for Galactic extinction. ^b Sérsic indexes. ^c Converted from Dunlop et al. (2003) Table 3 to our cosmology.

TABLE 2
LINE RATIOS OF 3C 79 LINE-EMITTING CLOUDS RELATIVE TO H β

Region	[Ne V] λ 3426	[O II] λ 3727	[Ne III] λ 3869	[O III] λ 4363	He II λ 4686	H β	[O III] λ 5007	[N I] λ 5199	H α	[N II] λ 6584
Gemini GMOS/IFU										
<i>a</i>	0.83 ± 0.19	2.45 ± 0.16	0.65 ± 0.07	0.15 ± 0.05	0.33 ± 0.04	1.00 ± 0.05	9.32 ± 0.03	< 0.18
<i>b</i>	1.54 ± 0.43	3.25 ± 0.35	1.18 ± 0.19	< 0.49	< 0.33	1.00 ± 0.11	8.91 ± 0.08	< 0.47
<i>c</i>	0.53 ± 0.10	2.50 ± 0.16	1.01 ± 0.05	0.13 ± 0.03	0.26 ± 0.02	1.00 ± 0.02	10.39 ± 0.02	0.06 ± 0.02
<i>d</i>	1.38 ± 0.15	2.62 ± 0.09	1.19 ± 0.05	0.19 ± 0.02	0.29 ± 0.02	1.00 ± 0.02	11.52 ± 0.01	0.05 ± 0.02
<i>NLR</i>	1.057 ± 0.016	1.590 ± 0.015	0.944 ± 0.004	0.176 ± 0.003	0.302 ± 0.003	1.000 ± 0.004	10.923 ± 0.002	0.041 ± 0.004
Keck LRIS/Long-Slit										
<i>N1</i>	0.60 ± 0.02	2.73 ± 0.02	1.09 ± 0.02	0.15 ± 0.03	0.28 ± 0.02	1.00 ± 0.02	10.63 ± 0.02	< 0.09	3.09 ± 0.03	1.24 ± 0.03
<i>S1</i>	0.58 ± 0.04	2.92 ± 0.05	1.31 ± 0.04	0.27 ± 0.07	< 0.15	1.00 ± 0.04	11.83 ± 0.03	< 0.21	2.93 ± 0.07	0.91 ± 0.06
<i>NLR</i>	1.093 ± 0.003	1.591 ± 0.015	0.921 ± 0.009	0.185 ± 0.008	0.297 ± 0.007	1.000 ± 0.008	10.602 ± 0.008	0.038 ± 0.017	3.100 ± 0.008	1.040 ± 0.007

TABLE 3
PROPERTIES OF 3C 79 LINE-EMITTING CLOUDS

Region	V (km s ⁻¹)	σ (km s ⁻¹)	A_V^a (mag)	H $\beta \times 10^{17}$ (erg cm ⁻² s ⁻¹)	[O II] 3726/3729	[O III] (4959+5007)/4363	N_e (cm ⁻³)	T_e (K)
<i>a</i>	-145	102	(0.000)	4.7 ± 0.2	...	85 ± 29
<i>b</i>	-138	91	(0.000)	1.4 ± 0.2	...	> 23
<i>c</i>	-74	109	0.016	21.0 ± 0.4	0.76 ± 0.08	108 ± 22	100 ± 100	12500^{+1200}_{-800}
<i>d</i>	+131	132	0.392	23.5 ± 0.4	0.80 ± 0.08	82 ± 10	150 ± 100	13900^{+800}_{-700}
<i>NLR</i>	0	136	0.284	99.6 ± 0.4	0.70 ± 0.07	83.0 ± 1.4	30 ± 80	13880 ± 100

^a Intrinsic reddening. The values in parentheses are not directly measured from the H γ /H β ratio, since the H γ lines in these spectra are not well-detected; and we assumed zero reddening for these clouds. See § 4.2.1 for details.